Universidad Carlos III de Madrid
e-Archivo

Institutional Repository

This document is published in:

Stability of nanoscale secondary phases in an oxide dispersion strengthened Fe 12Cr alloy

V. de Castro [a,*], E.A. Marquis [a,1], S. Lozano-Perez [a], R. Pareja [b], M.L. Jenkins [a]

[a] *Department of Materials, University of Oxford, Oxford OX1 3PH, UK*
[b] *Departamento de Física, Universidad Carlos III de Madrid, Avda. de la Universidad 30, 28911 Leganés, Madrid, Spain*

Abstract: Transmission electron microscopy and atom probe tomography were used to characterize on a near atomic scale the microstructure and oxide and carbide phases that form during thermo mechanical treatments of a model oxide dispersion strengthened Fe 12 wt.% Cr 0.4 wt.% Y_2O_3 alloy. It was found that some of the Y rich nanoparticles retained their initial crystallographic structure but developed a Cr enriched shell, while others evolved into ternary oxide phases during the initial processing. The Y and Cr rich oxide phases formed remained stable after annealing at 1023 K for 96 h. However, the number of Cr rich carbides appeared to increase, inducing Cr depletion in the matrix.

1. Introduction

The structural components of future fusion reactors will be subjected to high heat loads and neutron fluxes, imposing demanding requirements on materials used in such applications, including low activation, adequate strength and toughness, and high swelling and creep resistance [1]. Among the most promising candidate materials are reduced activation ferritic/martensitic (RAFM) steels [2]. Reduced activation in steels is achieved by replacing slow-decaying elements such as Nb, Mo and Ni with others that exhibit a higher decay rate of induced radioactivity, such as W and Ta [3]. High-temperature tensile strength and creep resistance in RAFM steels can be significantly improved by adding a very fine dispersion of Y_2O_3 parti-

cles, which prevent the motion of dislocations and provide a high density of pinning sites for grain boundaries, thereby stabilizing the microstructure at high temperatures. The high density of the particle matrix interfaces could also act as sinks for irradiation-induced defects and nucleation sites for helium bubbles, making these oxide dispersion strengthened (ODS) steels more resistant to radiation hardening and swelling [1]. ODS steels based on commercial RAFM steels, such as ODS 9 wt.% Cr Eurofer, ODS 14 wt.% Cr MA957 and 14YWT, are candidate materials for first wall components in the advanced blanket concepts that are being envisaged for the Demonstration Power Plant (DEMO) [4]. These steels are produced by powder metallurgy routes consisting of mechanical alloying (MA) of the starting powders followed by consolidation by hot isostatic pressing (HIP) or hot extrusion. In addition to Fe, Cr and a fine dispersion of nanoscale Y-rich oxides, these commercial steels contain other alloying elements such as V and Ta as stable carbide formers, W as a carbide former and solid-solution strengthener, and Ti to refine the grain and oxide particle sizes [5,6]. Moreover, impurity elements such as O and C are often unintentionally added

---

* Corresponding author. Present address: Departamento de Física, Universidad Carlos III de Madrid, Leganés, Spain. Tel.: +34 91624 9184; fax: +34 91624 8749.

E mail address: vanessa.decastro@uc3m.es (V. de Castro).

[1] Present address: Department of Materials Science and Engineering, University of Michigan, Ann Arbor, MI, USA.

owing to the nature of the production route, which could lead to the formation of unexpected complex phases with unknown behavior. The thermo-mechanical history is also crucial in defining the alloy microstructure, determining grain sizes and dislocation structures, the dispersion of fine oxide particles, and the size and distribution of oxides and carbides. This in turn affects mechanical behavior. For example, the ductile/brittle transition temperature of the first ODS Eurofer sheets produced by Plansee (Austria) was relatively poor, but a combination of hot rolling and subsequent austenitization and tempering enhanced the mechanical properties [7]. The poor fracture behavior of this ODS steel appeared to be due to the presence of fine $M_{23}C_6$ chromium carbides decorating the grain boundaries in the as-HIPed material [8]. Thus, both composition and thermo-mechanical history determine the mechanical response and irradiation behavior of the alloy.

Atom-probe tomography (APT) and transmission electron microscopy (TEM) analyses of a number of ODS steels have shown that the chemical composition and crystallographic structure of oxide nanoparticles can differ from that of the starting Y_2O_3 powders [9 12]. For exam-ple, oxide nanoparticles formed in Ti-containing MA/ODS steels are Y Ti O complexes [10 12]. Recent APT and electron energy loss spectroscopy (EELS) analyses of MA/ODS RAFM steels showed that some of the particles exhibited a core shell structure consisting of a complex Y-rich core surrounded by a Cr- and V-rich shell [13,14]. I t i s not clear whether this core shell structure has a crystallo-graphic phase different from that of the starting Y_2O_3. Mechanical properties, as well as particle behavior under irradiation, could change significantly depending on the structure of the nanoparticles. In consequence, understand-ing the effect of the impurities and alloying elements on the stability and structure of these dispersoids is crucial for developing ODS RAFM steels.

The purpose of the present work was to investigate the nature, microstructural characteristics and thermal stabil-ity of the dispersoids and grain microstructure in a model MA ODS/Fe 12 wt.% Cr alloy. This material is less com-plex metallurgically than commercial steels, making it eas-ier to investigate the evolution of oxide and carbide phases during fabrication and their subsequent stability under thermal treatments.

2. Experimental methods

The nominal composition of the model ODS alloy was Fe 12Cr 0.4Y_2O_3 wt.% (Fe 12.8Cr 0.2Y 0.3O at.%). The starting metallic powders were 99.5% pure Fe and 99% pure Cr (Alfa Aesar), with sizes <10 μm and 45 μm, respectively. The Y_2O_3 starting powder (Pi-Kem) was spherical, with sizes ranging from ∼5 to 50 nm. The lattice parameters of the powders were obtained from X-ray dif-fraction measurements. The diffraction peaks were consis-tent with a monoclinic cell as characterized in Ref. [15]. The ODS alloy, as well as a non-ODS Fe12Cr reference

alloy, were produced by MA followed by HIP, as described in Ref. [16]. The MA of the elemental Fe and Cr powders was performed in argon in a Union Process vertical attri-tion mill at a speed of 300 rpm for 15 h. A ball-to-powder ratio of 20:1 was used. The materials used inside the attri-tor chamber were AISI 52100 hardened steel grinding balls of Ø3/16-in., 304 SS for the vessel, shaft and bar grid and 440C SS for the rotor arms. The dispersion of 0.4 wt.% Y_2O_3 was accomplished by the corresponding addition fol-lowed by further milling for 12 h under the same condi-tions. The ODS and non-ODS batches were canned and degassed for 10 h at 623 K in vacuum. The sealed cans were HIPed at 1373 K under a pressure of 190 MPa for 2 h and cooled down at a rate of 30 K min ^{1}. The alloys were subsequently annealed at 1023 K for 4, 24 and 96 h and furnace cooled in vacuum. Samples of these alloys in the as-HIPed condition and after the thermal treatments were analysed by analytical TEM and APT.

The samples for TEM were prepared by electropolishing 3-mm-diameter disks in a TENUPOL 5 twin-jet polisher using 5% $HClO_4$ + 95% CH_3OH as electrolyte. Before each TEM session, the samples were also cleaned at 1.5 kV for a few minutes in an ion beam thinner. TEM bright-field (BF) imaging and diffraction characterization was carried out on a Philips CM20 instrument operated at 200 kV and equipped with an X-ray energy dispersive spectrometer. High resolution electron microscopy (HREM) images, high angle annular dark field (HAADF) scanning TEM (STEM) images, X-ray energy dispersive spectrometry (XEDS) and EELS elemental maps were obtained using a JEOL 3000F microscope operated at 297 kV. Energy filtered TEM (EFTEM) maps were obtained with a JEOL 2200MCO prototype microscope operated at 200 kV equipped with two spherical aberration (C_s) correctors and an Ω-filter. The EFTEM series were processed after acquisition using multivariate statistical analysis (MSA) in order to remove the noise, as described elsewhere [17].

The samples for APT were prepared by standard elec-tropolishing methods [18], and the analyses carried out with LEAP-3000X and 3000XHR atom-probe micro-scopes. During the analyses, the tips were maintained at 30 60 K for field evaporation using either voltage pulsing (20% pulse fraction, 200 kHz) or laser pulsing (wavelength 532 nm, pulse width 10 ps, repetition rate 200 kHz, energy ∼0.2 4 nJ and spot size ∼10 μm).

3. Results and discussion

The general microstructure of the as-HIPed materials was reported in Ref. [16]. Both reference and ODS alloys exhibited a martensite lath grain structure with a lath width of ∼100 400 nm and a high density of dislocations.

The C and O contents in the reference and ODS alloys were determined by IR absorption. The measured C concentrations were (0.32 ± 0.07) at.% and (0.41 ± 0.09) at.%, respectively. These C contents are similar to those found in low carbon steels such as Eurofer [19].

The C concentration specified in the certificate of analysis of the starting Fe powders was 0.24 at.%. The excess C in the alloys is attributed to the intake from the grinding media and chamber used for MA. The O concentrations were found to be (1.4 ± 0.7) at.% for the reference alloy and (2.0 ± 0.7) at.% for the ODS alloy. These O contents are consistent with the O concentrations of the starting powders ($\sim$1.3 at.%), and indicate that there was little or no air intake during the powder processing.

The alloys contained several different types of secondary phases. Large Cr-rich oxides and carbides with sizes <1 μm were found in both alloys. In addition, the ODS alloy contained an inhomogeneous distribution of smaller Y-rich particles with sizes <50 nm. Coherent precipitates, identified as cementite carbides, were also observed on the as-HIPed alloys, but disappeared after annealing [16].

3.1. General microstructures

The effects of annealing at 1023 K on the microstructures of the ODS/Fe 12Cr and reference Fe 12Cr alloys are shown in the BF micrographs of Fig. 1. Fig. 1a c shows the ODS/Fe 12Cr alloy after annealing for 4, 24 and 96 h, respectively. No significant changes in the grain micro-

structure were observed, apart from a partial grain recovery in some areas of the samples. This inhomogeneous recovery seems to be a direct consequence of the inhomogeneous distribution of Cr-rich precipitates and Y-rich nanoparticles, since evidence for recovery and recrystallization was found only in areas depleted of such particles. These areas, marked "R" in Fig. 1, consist of almost dislocation-free equiaxed grains with sizes <2 μm. In these recovered areas, secondary phases are observed at grain boundaries suggesting grain boundary pinning.

For the ODS/Fe 12Cr alloy, the areas that remained unrecovered (those marked "U" in the images of Fig. 1) contained very high densities of small secondary phase particles. Previous work showed that nanoparticles in ODS alloys are effective sites for trapping dislocations [20,21]. Some of these areas contained submicron-sized grains with either lath or equiaxed morphologies. In other areas, the grain morphology could not be clearly distinguished owing to the high density of dislocations.

In order to discriminate the capability of the Cr-rich and Y-rich precipitates to inhibit grain growth and dislocation annealing, an analysis of the reference Fe 12Cr alloy was performed. Fig. 1d shows a BF micrograph of a representative region from this reference alloy heat-treated at
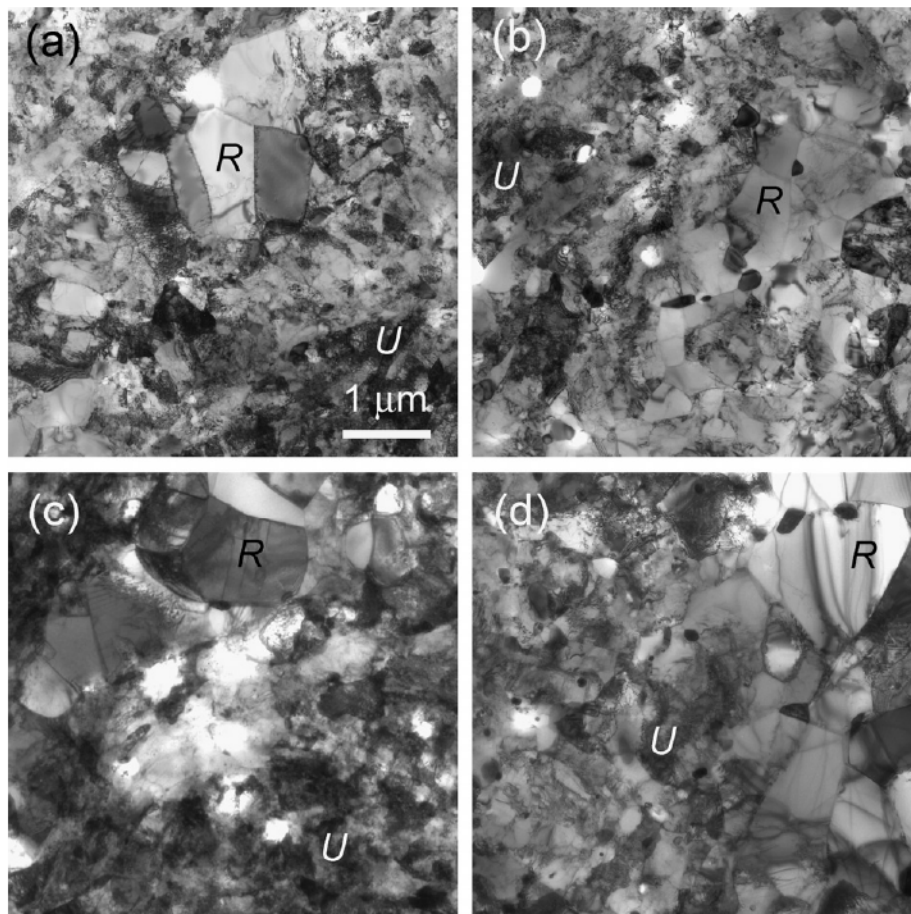

Fig. 1. Effect of heat treatments on the grain microstructure of (a c) the ODS/Fe 12Cr and (d) the reference Fe 12Cr alloy. The alloys were annealed at 1023 K for (a) 4 h, (b) 24 h and (c), (d) 96 h. R and U mark recovered and unrecovered regions, respectively (see text).

1023 K for 96 h. The grain microstructure, with recovered (R) and unrecovered areas (U), appears similar to that of the ODS alloy. These results indicate that Cr-rich particles, i.e., oxides and carbides, which are present in both alloys, have the capability to inhibit grain growth and dislocation annealing. However, more detailed observations revealed some qualitative differences between the two alloys: (1) grains and grain boundaries were usually clearly distinguishable in the reference Fe12Cr samples, while a high dislocation density accumulated in many areas of the ODS alloy samples and prevented a clear visualization of the microstructure; and (2) the recovered areas were less uniformly distributed in the ODS alloy. These differences appear to be directly associated with the inhomogeneous distribution of the Y-rich nanoparticles, since the unrecovered areas which exhibited a very high dislocation density with indistinguishable grains also had a very high density of these particles, as the analyses reported in Section 3.3.2 reveal. The inhomogeneous distribution of the Y-rich nanoparticles may be attributed to an insufficient optimization of the milling process.

APT analyses of the ODS/Fe 12Cr matrix revealed compositional changes induced by heat treatments at 1023 K. As shown in Table 1, C and Cr depletion in the matrix after the first heat treatment was perceptible. This is consistent with the formation of Cr-rich carbides. After this treatment, the measured Cr content did not vary significantly with increasing annealing time. Reduction of the C content after subsequent treatments could be due to C segregation at grain boundaries, as reported in Ref. [22]. The O content in the matrix did not vary significantly, suggesting that the oxides formed in the alloy are stable phases. The N content varied between $\sim$0.05 and 0.2 at.%, depending on the sample.

3.2. Large Cr-rich oxide and carbide phases

3.2.1. Phase identification

Chemical analysis of the large precipitates was performed by TEM using XEDS and EELS for point analyses and elemental mapping, as well as by APT. All the large precipitates analysed were Cr-rich carbides or oxides. Fig. 2a c shows a HAADF-STEM image and the corresponding XEDS elemental maps of two of these Cr-rich precipitates in the ODS alloy annealed for 4 h at 1023 K. Atom-probe reconstructions of both precipitate types in

an ODS alloy specimen heat-treated for 96 h are also shown in Fig. 2d. The Cr carbide shown on the left in Fig. 2d had composition 17.4 19.4 at.% C, 56.1 57.4 at.%Cr and 24.6 25.2 at.% Fe; the uncertainties arise from the ambiguity in assigning the C peaks in the mass spectrum. This composition is consistent with an $M_{23}C_6$ carbide where M Cr, Fe with an Fe/Cr ratio 0.45 0.5. It should be noted that a somewhat lower measurement of the C content by APT is expected, owing to the loss of information through multiple events or evaporation between pulses [23]. The maximum solubility of Cr in $(Cr, Fe)_{23}C_6$ is $\sim$51 at.% according to Ref. [24], yielding a Fe/Cr ratio of 0.56, which is slightly higher than that measured here. However, it has been reported than the Cr content of $M_{23}C_6$ carbides increases with annealing time, resulting in lower Fe/Cr ratios. For example, Fe/Cr ratios for $M_{23}C_6$ precipitates as low as $\sim$0.2 at.% have been reported in an AISI 304 stainless steel annealed at 923 K for 48 h [25], and ratios of 0.36 0.39 at.% were found in T91 and E911 steels after normalizing and tempering [26].

Analysis of the adjoining Cr-rich oxide on the right in Fig. 2d revealed a composition of 40 ± 1 at.% Cr, 7 ± 1 at.% Fe, and 54 ± 1 at.% O, which is somewhat oxygen-deficient compared with the Cr_2O_3 phase. Al was segregated at the particle/matrix interface. The presence of Al probably comes from the Cr powders, which contain $\sim$0.004 at.% Al.

Selected-area and convergent-beam diffraction patterns, along with HREM images, were also used to determine the crystal structure of the Cr-rich precipitates and verify the results obtained from the analytical measurements. The structural information (interplanar spacings and angles) obtained from the diffraction patterns and Fourier transforms of the HREM images of precipitates in zone-axis orientations was compared with those of the most common stable Cr oxides and carbides found in the literature, i.e., Cr_2O_3 oxide, $M_{23}C_6$ (M Cr, Fe), Cr_3C_2 and Cr_7C_3 carbides, and $CrFe_2O_4$ spinel. Cr_2N and CrN nitrides were also considered because of the high measured N content. The crystal structures of these precipitates were obtained from the Chemical Database Service [27]. More than 75%of the precipitates could be indexed as either $M_{23}C_6$ or Cr_2O_3. HREM images of these phases are shown in Fig. 3. Other precipitates investigated could be indexed as Cr_3C_2 or Cr_2N. The presence of other phases containing Al should not be excluded because of the detected Al impurities.

3.2.2. Effect of heat treatments

The size distributions and mean sizes of the large precipitates after the three heat treatments are shown in Fig. 4. The precipitates did not appear to grow significantly on annealing at 1023 K, at least up to 96 h. Most of them had sizes ranging from $\sim$ 50 to 500 nm, although some precipitates larger than 1 μm were observed in the alloy annealed for 96 h. Although $M_{23}C_6$ coarsening might be expected for temperatures above $\sim$923 K [28], there are

Table 1
Variation in the chemical composition of the ODS/Fe 12Cr matrix through annealing at 1023 K; the compositions (in at.%) were measured from APT analyses.

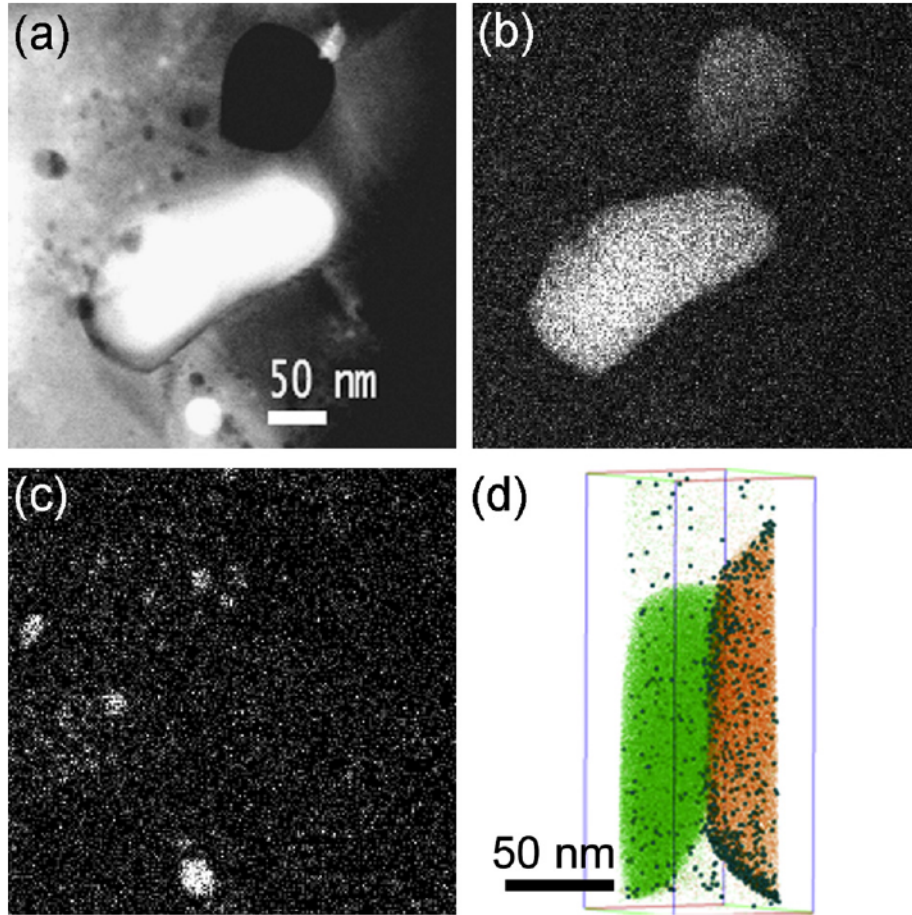|	As HIPed	After 4 h	After 24 h	After 96 h
C	0.25 ± 0.09	0.07 ± 0.01	0.02 ± 0.01	0.02 ± 0.01
Cr	10.7 ± 0.8	9.2 ± 0.9	9.5 ± 0.9	9.6 ± 0.9
O	0.10 ± 0.08	0.10 ± 0.08	0.3 ± 0.2	0.2 ± 0.1
N	0.20 ± 0.06	0.05 ± 0.03	0.10 ± 0.06	0.20 ± 0.07

Fig. 2. STEM images of the ODS/Fe 12Cr alloy annealed for 4 h at 1023 K: (a) HAADF STEM image and corresponding (b) Cr and (c) Y XEDS maps; (d) APT reconstruction of the ODS/Fe 12Cr alloy annealed for 96 h showing a Cr rich carbide (left side) and a Cr oxide (right side) presenting Al segregation to the interface. The reconstruction shows C, O and Al atoms.
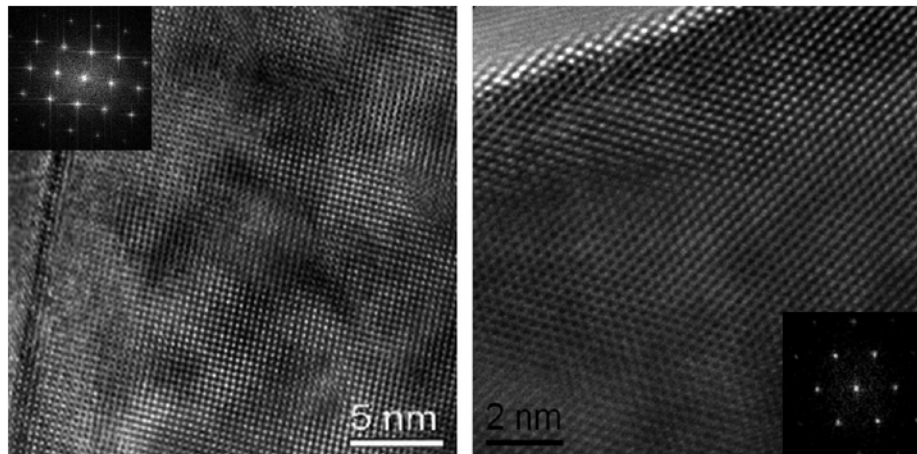

Fig. 3. HREM images of Cr rich precipitates indexed as (a) $M_{23}C_6$ (M = Cr, Fe) oriented on the $\langle 100 \rangle$ zone axis and (b) Cr_2O_3 oriented on the [0 0 1] zone axis.

reports showing that this coarsening may not be significant for steels with C and Cr contents similar to or higher than the present alloys heat-treated under similar conditions [25,29].

The number densities of large precipitates for the ODS/Fe 12Cr in as-HIPed condition and after annealing at

1023 K for four and 96 h were estimated from measurements on TEM foils in regions with average volumes of $5 \times 5 \times 0.2\ \mu m^3$. The foil thickness was calculated using the log-ratio technique [30]. The inelastic mean free path was estimated from the formula derived by Malis et al. [31]. In all cases, measurements were made in foils of
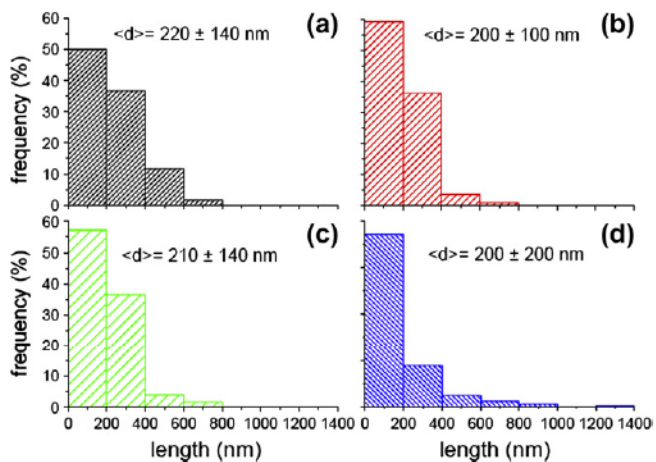
Fig. 4. Histograms showing the size distribution of the Cr rich oxides and carbides for the ODS/Fe 12Cr (a) as HIPed, (b) annealed for 4 h, (c) annealed for 24 h and (d) annealed for 96 h, all at 1023 K.

similar thickness in order to minimize relative errors due to over-counting of precipitates larger than the foil thickness. The measured densities in all samples varied between $1.0 \pm 0.2 (\times 10^{19})$ m $^{-3}$ and $3.0 \pm 0.6 (\times 10^{19})$ m $^{-3}$, depending on the region. No significant changes were observed in the densities with increasing annealing time. This would imply that these precipitates are quite stable during heat treatment at 1023 K. However, density measurements could be misleading owing to the heterogeneous precipitation of the Cr-rich phases, which frequently nucleate on pre-existing precipitates. Indeed, the matrix Cr and C

contents shown in Table 1 are consistent with the formation of Cr-rich carbides after the first heat treatment, as previously discussed in Section 3.1. Moreover, the number of precipitates indexed as $M_{23}C_6$ carbides increased significantly after annealing for 4 h, but with no subsequent changes at longer annealing times.

3.3. Small Y- and Cr-rich oxide phases

3.3.1. Phase identification

The chemical compositions of the particles were investigated by STEM XEDS and EELS, EFTEM and APT. Nanoparticles with different chemical compositions were found. Some of the nanoparticles consisted of a Y O-rich core and a Cr-rich shell, as shown in Fig. 5. Similar core shell structured particles have recently been observed in different ODS steels, the composition of the shell depending on the elements present in the steel [32]. The Cr-rich shells had thicknesses of ~1 3 nm in the ODS alloy annealed for 4 h [32,33]. The shell was still present after annealing for 24 and 96 h. EFTEM analyses performed on eight different regions with average volumes of $300 \times 300 \times 100$ nm^3 in the ODS alloy heat-treated for 96 h showed no significant changes in the shell thickness. EELS and XEDS elemental profiles, as well as intensity profiles from EFTEM maps performed across selected particles for the alloys heat-treated for 24 and 96 h, revealed that the Cr signal extended further into the matrix than the Y and O signals; see Fig. 5c e, for example. It is concluded from these observations that the Cr shell is not
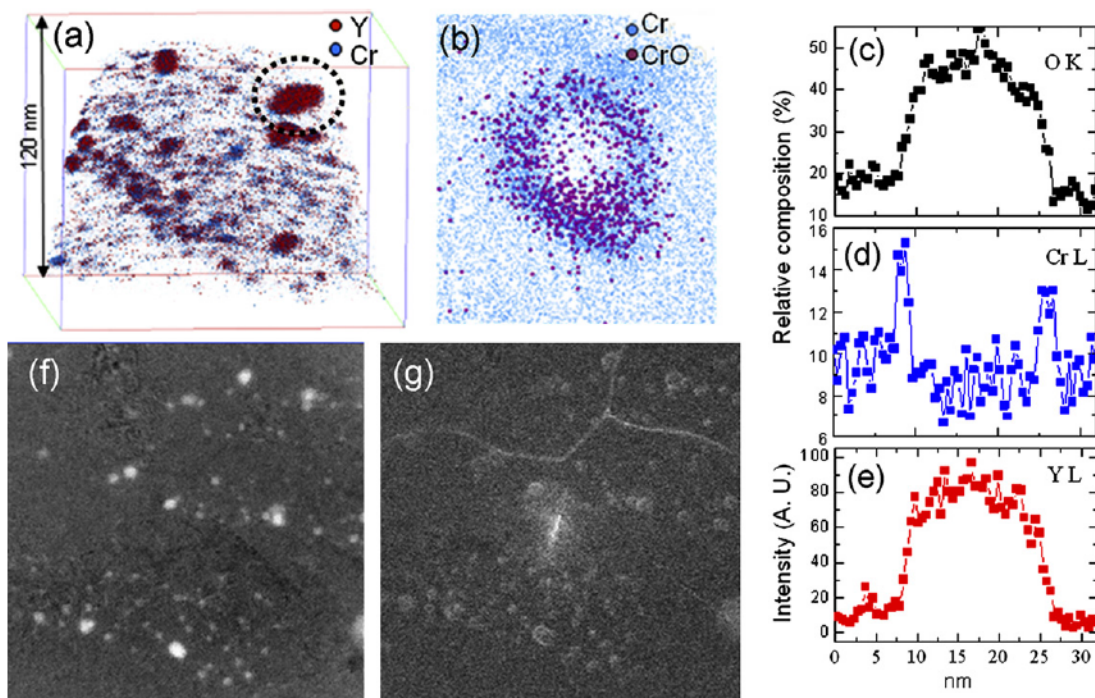

Fig. 5. (a and b) APT reconstructions showing Y and Cr atoms for the ODS alloy after 4 h annealing; (b) shows the Cr rich shell from the particle marked in (a). (c and d) EELS and (e) EDS O K, Cr L and Y L elemental profiles across a nanoparticle in the ODS alloy after 24 h annealing. (f and g) Y N$_{2,3}$ and Cr L$_{2,3}$ EFTEM elemental maps for the ODS alloy after 96 h annealing.

totally oxidized. These results confirm the APT observations for the ODS alloy heat-treated for 4 h [32]. The shell could result from Cr segregation at the particle matrix interface. Cr segregation was also frequently observed at grain boundaries (Fig. 5g) [34].

Other particles exhibited a more homogeneous Y Cr O structure in the central region, with no distinct Cr-rich shell (see Fig. 6). However, in at least some of these particles, the Cr signal extended further into the matrix than the Y signal did (Fig. 6e and f). The atom-probe data obtained from the particle in Fig. 6g shows one of these Y Cr O particles with measured composition: 27 ± 1 at.% Cr, 25 ± 1 at.% Y, 48 ± 1 at.% O. Nanoparticles with sizes similar to the Y-rich ones, but containing only Cr and O, were also detected. Fig. 6 also shows such particles (arrowed) in the ODS/Fe 12Cr after 96 h. There was no evidence for small Cr O nanoparticles in the as-HIPed samples, but they were observed after the 4 h treatment [35].

The Y Cr O structured nanoparticles could have formed during the initial synthesis of the alloy, owing to partial dissolution of the starting Y_2O_3 during MA, followed by precipitation of Y, O and Cr during HIP. Y_2O_3 has a lower Gibbs energy of formation than ternary oxides, such as $YCrO_3$ [36]. However, the ternary Y Cr O phase diagram, also described in Ref. [36], shows that Y_2O_3 can coexist with $YCrO_3$ at temperatures comparable with the HIP temperature of 1373 K. HREM studies were performed in an attempt to determine whether these or other possible crystallographic phases appeared in the alloys. X-ray (Section 2) and HREM analyses showed that the starting Y_2O_3 powders were monoclinic. Fig. 7a shows one of these powder particles oriented on the [1 1 0] zone axis of monoclinic Y_2O_3. Although the body-centered cubic (bcc) phase of bulk Y_2O_3 is the most stable

polymorph at atmospheric pressure and up to 2598 K [37,38], nanometric Y_2O_3 particles are thermodynamically stable in the monoclinic phase owing to the increasing importance of surface effects [39].

The crystallographic information (interplanar spacings and angles) obtained from Fourier transforms of HREM images of Y-rich particles in zone-axis orientations was compared with the structural data of several candidate structures. These included monoclinic and bcc Y_2O_3, a s well as $YCrO_4$ and orthorhombic $YCrO_3$. Data for these structures were obtained from the Chemical Database Service [27]. The pyrochlore $Y_2Cr_2O_7$ was not considered, as it requires both high pressure and high temperature to be formed [40]. The bcc Y_2O_3 was considered because Y O particles could have re-precipitated in the cubic phase, which is expected to be more favorably embedded into a bcc matrix. The MA process may induce the mono-clinic $\rightarrow$ bcc transformation, either directly by plastic deformation or via dissolution of the starting Y_2O_3 and re-precipitation, during MA, as bcc particles. The crystal structures for $YCrO_4$ and $YCrO_3$ are described in Ref.[41]. Y C r O $_3$ exhibits two phases, orthorhombic and rhom-bohedral. However, the rhombohedral phase is not expected, as it is stable only above $\sim$1200 K [42]. More-over, $YCrO_4$ particles could be transformed into $YCrO_3$ during the heat treatments, since this transformation can occur over the temperature range 1023 1083 K [41,42].

After HIP consolidation and annealing at 1023 K, $\sim$30% of the analysed nanoparticles could still be indexed as monoclinic Y_2O_3; see the example in Fig. 7b. About 10% of the particles seemed to correspond to $YCrO_3$. One of these particles is shown in Fig. 7c. The other analysed particles could not be clearly indexed as any of the other known Y O or Y Cr O phases mentioned above,
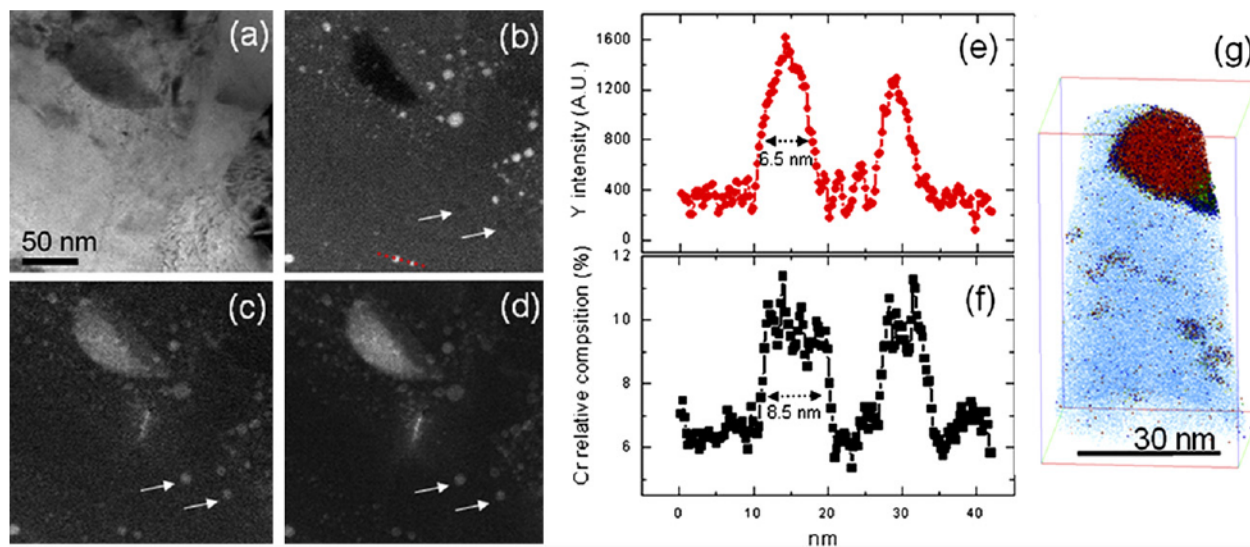

Fig. 6. (a d) EFTEM series showing nanoparticles with different compositions in the ODS alloy annealed for 96 h: (a) BF image; (b) Y $N_{2,3}$; (c) O K; (d) Cr $L_{2,3}$ EFTEM elemental maps. The particles marked with an arrow in the elemental maps contain Cr and O but no Y. (e) Y and (f) Cr intensity profiles across two of the Y rich particles (see dashed line) reveal that the Cr signal extends further than the Y signal. (g) APT reconstruction of the as HIPed ODS alloy showing a particle with a homogeneous Y Cr O distribution.
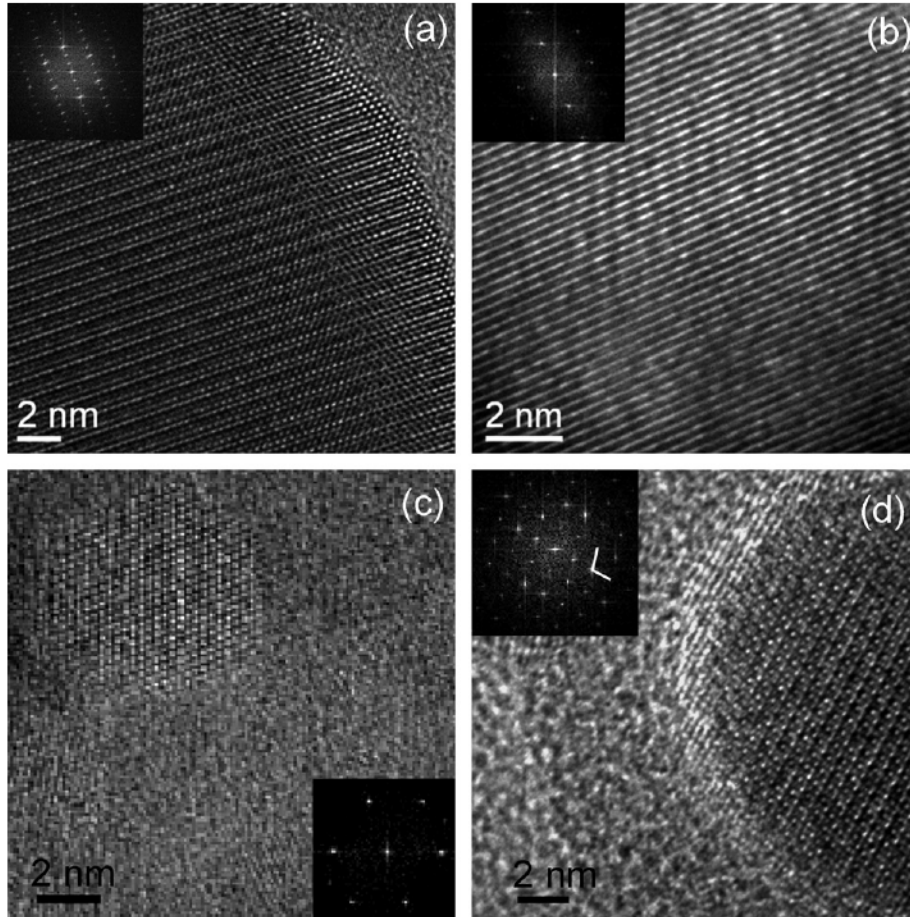
Fig. 7. HREM images of (a) one of the starting Y_2O_3 powder nanoparticles oriented on the [1 1 0] zone axis of monoclinic Y_2O_3 and (b d) nanoparticles in the consolidated ODS alloys: (b) Y rich nanoparticle for the ODS alloy annealed for 24 h, which can be indexed as monoclinic Y_2O_3 oriented on the [5 1 2] zone axis; (c) Y rich nanoparticle for the ODS alloy annealed for 4 h, which can be indexed as $YCrO_3$ oriented on the [2 4 1] zone axis; (d) unknown nanoparticle for the as HIPed ODS alloy. The measured interplanar spacings ($d_1 = (5.5 \pm 0.3)$ Å and $d_2 = (5.9 \pm 0.3)$ Å) are marked in the Fourier transform of the HREM image.

there being a mismatch in respect of the theoretical spacings and angles of these phases higher than ~30% in all cases. Other possible phases that could arise from the presence of impurities such as Al, N or C (in particular $YAlO_3$, YN, Y_2C, Y_2C_3 and YC_2) were also considered, but no satisfactory fits were obtained. An example of one of these unknown particles is shown in Fig. 7d. The particle could not be indexed as any of the possible compounds mentioned above. The two interplanar spacings measured from the Fourier transform (see Fig. 7d) were d_1 (5.5 ± 0.3) Å and d_2 (5.9 ± 0.3) Å, and they subtend an angle of ~105°. These spacings are too high for the particle to be YC_2, Y_2C or $YAlO_3$. When trying to index it as $YCrO_3$, $YCrO_4$ or monoclinic Y_2O_3, the indexation error was >30%. The interplanar spacings and angles measured would match a bcc Y_2O_3 structure on the [3 2 1] zone axis (with an indexation error of ~15%). However, both (1 1 1) and (0 1 2) planar families should be extinct in this structure.

Possible effects leading to erroneous indexation include the presence of double diffraction spots in the pattern due

to either particle matrix overlap or interaction with a thin oxide layer which frequently forms on the samples [43]. Moreover, the presence of surface strains or incomplete surface layers in nanoparticles could produce additional diffraction spots [44]. Another possibility is the presence of a non-equilibrium phase. The composition measured by APT suggests the formation of $YCrO_2$. Y is generally found in an oxidation state of $+3$, although an oxidation state of $+2$ is also possible [45]. Cr can adopt a valence of $+2$, which would allow this oxide to form. However, no evidence of such an oxide has been reported in the liter-ature. The oxygen content measured by APT could be underestimated owing to possible loss during evaporation. However, the possibility that this oxide is present cannot be excluded.

The coherence of the particles could not be studied in detail, as the TEM samples' surface often lacked the desired thickness homogeneity. Fast surface oxidation of the ferritic matrix was also an issue, but first results show that the analysed particles do not seem to exhibit an orientation relationship with the matrix. These observations are
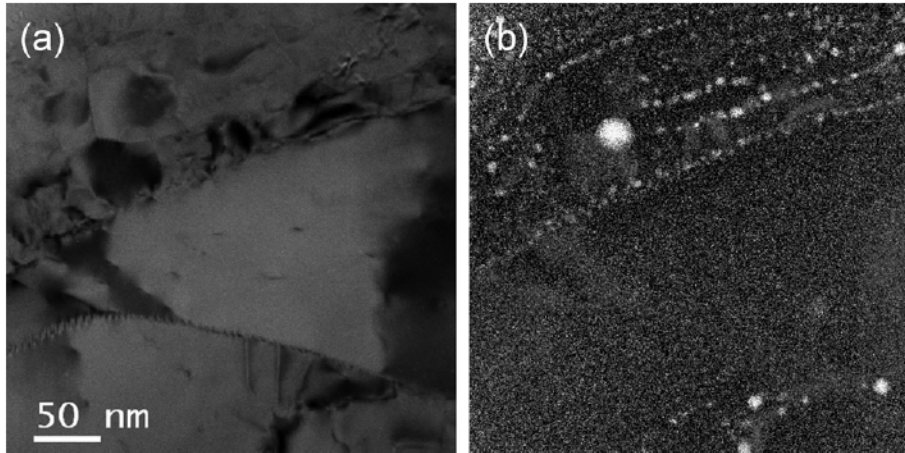
Fig. 8. (a) BF image and (b) corresponding Y $N_{2,3}$ EFTEM map of the ODS/Fe12Cr annealed for 4 h showing the inhomogeneous distribution of Y rich particles.
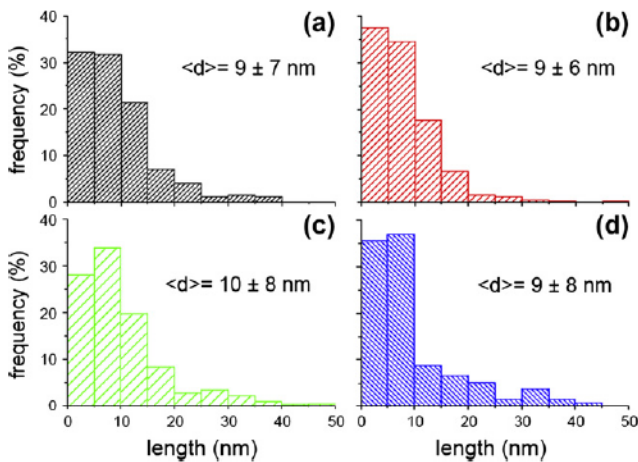

Fig. 9. Size distribution of the small Y and Cr rich oxide nanoparticles for the ODS/Fe 12Cr (a) as HIPed, (b) annealed for 4 h, (c) annealed for 24 h and (d) annealed for 96 h.

in agreement with the general microstructure observed, as incoherent particles may be difficult to shear by dislocations, preventing their annealing.

3.3.2. Effect of heat treatments

Initially, the Y-rich nanoparticles were distributed quite inhomogeneously in the alloys. This remained so after annealing. Fig. 8 shows Y-rich particles in a sample annealed for 4 h. Many were aligned along grain boundaries, including a boundary separating a recovered from an unrecovered region. Most of the recovered areas and new sub-boundaries formed within recovered areas were free of nanoparticles, but not all. In unrecovered regions, the particles were mainly distributed within the grains, but they were also observed at grain boundaries and pinning dislocations [16].

The densities and volume fractions of nanoparticles in representative unrecovered regions were determined by TEM. EFTEM analyses were performed in 10 different

areas of size $\sim300 \times 300 \times 100$ nm^3. Densities ranged between 4.5 ± 0.9 ($\times10^{21}$) m^{-3} and 1.2 ± 0.2 ($\times10^{23}$) m^{-3}. No significant changes in density were observed with annealing time. The volume fractions were estimated assuming spherical morphologies, leading to values between 0.14 ± 0.03 and 2.3 ± 0.5 vol.%.

The overall particle size distribution is depicted in Fig. 9. These histograms were obtained by measuring more than 300 particles in different regions of the samples. The particle sizes appeared to remain stable at 1023 K, at least for 96 h.

4. Conclusions

The thermal stability of the microstructure of an ODS/Fe 12Cr model alloy was investigated by analytical electron microscopy and 3D-APT. The main conclusions are:

1. The grain structure and particle dispersion were stable under heating at 1023 K for 96 h.
2. Nanometric Y Cr-rich and submicron Cr-rich particles of secondary phases were distributed heterogeneously in the alloy. These particles prevent recovery and recrystallization by effectively pinning dislocations and grain boundaries, but appear to be responsible for an inhomogeneous grain recovery. This might have some detrimental effect on the mechanical performance of the alloy.
3. Most of the Cr-rich particles corresponded to Cr_2O_3 oxides and $M_{23}C_6$ (M   Cr, Fe) carbides. Analyses of the Y Cr-rich particle structure confirm that some of the nanoparticles have retained the initial Y_2O_3 monoclinic structure, but also suggest that in other cases new crystallographic phases such as $YCrO_3$ have developed.
4. Y Cr- and Cr-rich oxides remained stable at 1023 K for 96 h, but the proportion of Cr-rich carbides increased, inducing Cr depletion in the matrix. This should result in a reduction of the oxidation and corrosion resistance of the alloy.

5. The Y Cr-rich oxides developed either a core shell structure with a Cr-enriched shell, or a structure with the Y, Cr and O atoms homogeneously distributed. The core shell structured particles could correspond to the Y_2O_3 particles, with the Cr shell resulting from Cr diffusion towards the particle matrix interface. The homogeneous Y Cr O particles could correspond to $YCrO_3$ or could be non-equilibrium phases. Since oxide particles with differences in composition or structure may exhibit very different behavior under high-flux irradiation, this may be a critical issue if this type of alloys is used as a structural material in advanced fusion reactors.

Acknowledgements

References

[1] Odette GR, Alinger MJ, Wirth BD. Annu Rev Mater Res 2009;38:471.

[2] Moslang A. Proceedings of ITER, une étape majeure vers l'énergie de fusion nucleaire 2007;1:96.

[3] Boutard JL, Alamo A, Lindau R, Rieth M. CR Physique 2008;9:287.

[4] Diegele E, Andreani R, Lasser R, van der Schaaf B. Fusion Sci Technol 2005;47(4):829.

[5] Klueh RL. Report ORNL/TM 2004/ 176, Oak Ridge National Laboratory, Oak Ridge, TN, USA; 2004.

[6] Schneibel JH, Liu CT, Hoelzer DT, Mills MJ, Sarosi P, Hayashi T, et al. Scripta Mater 2007;57:1040.

[7] Lindau R et al. Fusion Eng Des 2005;75 79:989.

[8] Klimiankou M, Lindau R, Moslang A. J Nucl Mater 2007;367 370:173.

[9] Klimiankou M, Lindau R, Moslang A, Schroder J. Powder Metall 2005;48(3):277.

[10] Miller MK, Kenik EA, Russell KF, Heatherly L, Hoelzer DT, Maziasz PJ. Mater Sci Eng, A 2003;353:140.

[11] Miller MK, Hoelzer DT, Kenik EA, Russell KF. Intermetallics 2005;13:387.

[12] Alinger MJ, Odette GR, Hoelzer DT. Acta Mater 2009;57:392.

[13] Williams C, Marquis EA, Cerezo A, Smith GDW. J Nucl Mater 2010;400:37.

[14] Klimenkov M, Lindau R, Moslang A. J Nucl Mater 2009;386 388:553.

[15] de Castro V, Leguey T, Monge MA, Munoz A, Pareja R, Amador DR, et al. J Nucl Mater 2003;322:228.

[16] de Castro V, Leguey T, Munoz A, Monge MA, Pareja R, Marquis EA, et al. J Nucl Mater 2009;386 388:449.

[17] Lozano Perez S, de Castro Bernal V, Nicholls RJ. Ultramicroscopy 2009;109:1217.

[18] Miller MK, Cerezo A, Hetherington MG, Smith GDW. Atom probe field ion microscopy. New York: Oxford University; 1996.

[19] Schaeublin R, Leguey T, Spatig P, Baluc N, Victoria M. J Nucl Mater 2002;307 311:778.

[20] Zakine C, Prioul C, Francois D. Mater Sci Eng, A 1996;A219:102.

[21] Preston J, Wilshire B, Little EA. Scripta Metall Mater 1991;25:183.

[22] Marquis EA, Lozano Perez S, de Castro V. J Nucl Mater, in press. doi:10.1016/j.jnucmat.2010.12.251.

[23] Sha W, Chang J L, Smith GDW, Cheng L, Mittemeijer EJ. Surf Sci 1992;266:416.

[24] Minkoff I. The physical metallurgy of cast iron. Chichester: John Wiley; 1983. p. 180.

[25] Boeuf A, Coppola R, Rustichelli F, Zambonardi F. J Appl Crystal logr 1981;14:337.

[26] Orr J, Woollard L. In: Strand A, Gooch DJ, editors. Microstructural development and stability in high chromium ferritic power plant steels, The Institute Materials, London, Book 667; 1997.

[27] Fletcher DA, McMeeking RF, Parkin D. J Chem Inf Comput Sci 1996;36:746.

[28] Klueh RL, Harries DR, Physical metallurgy of high chromium steels in: high chromium ferritic and martensitic steels for nuclear applica tions. ASTM; 2001. p. 28.

[29] Hattestrand M, Andrén H O. Mater Sci Eng A 2001;318:94 101.

[30] Williams DB, Carter CB. Microanalysis with ionization loss elec trons. In: Transmission electron microscopy. New York: Plenum Press; 1996. p. 678.

[31] Malis T, Cheng SC, Egerton RF. J Electron Microsc Tech 1988;8:193.

[32] Marquis EA. Appl Phys Lett 2008;93:181904.

[33] de Castro V, Lozano Perez S, Jenkins ML. MRS Proc 2009;1125:R07.

[34] Marquis EA, Hyde JM, Saxey DW, Lozano Perez S, de Castro V, Hudson D, et al. Mater Today 2009;12 11:30 8.

[35] de Castro V, Lozano Perez S, Jenkins ML. JOP: Conf Series 2010;241(012107):1 4.

[36] Kawamura K I, Maruyama T, Nagata K. Metall Mater Trans B 1995;26B:289.

[37] Binary Alloys and Phase Diagrams. ASM; 1990. p. 2936.

[38] Pauling L, Shappel MD. Z Kristallogr 1930;75(1 2):128.

[39] Guo B, Luo Z P. J Am Ceram Soc 2008;91 95:1653.

[40] Matteucci F, Cruciani G, Dondi M, Baldi G, Barzanti A. Acta Mater 2007;55(7):2229.

[41] Bedekar V, Shukla R, Tyagi AK. Nanotechnology 2007;18:155706.

[42] Tachiwaki T, Kunifusa Y, Yoshinaka M, Hirota K, Yamaguchi O. Int J Inorg Mater 2001;3:107.

[43] Williams DB, Carter CB. Indexing diffraction patterns. In: Trans mission electron microscopy. New York: Plenum Press; 1996. p. 265.

[44] Reyes Gasga J, Gómez Rodríguez A, Gao X, José Yacamán M. Ultramicroscopy 2008;108:929.

[45] Gibson PN, Cristobal MJ, Stroosnijder MF. J Phys IV France 1997;7:C2 1205.